



# Two-color frequency-multiplexed IMS technique for gas thermometry at elevated pressures

Wei Wei<sup>1</sup> · Wen Yu Peng<sup>1</sup> · Yu Wang<sup>1</sup> · Jiankun Shao<sup>1</sup> · Christopher L. Strand<sup>1</sup> · Ronald K. Hanson<sup>1</sup>

Received: 25 July 2019 / Accepted: 11 February 2020 / Published online: 2 March 2020  
© Springer-Verlag GmbH Germany, part of Springer Nature 2020

## Abstract

The development and demonstration of a high-bandwidth two-color temperature sensor for high-pressure environments using intensity-modulation spectroscopy (IMS) is presented. The sensor utilized rapid intensity modulation, beam coalignment, and frequency multiplexing to deal with common challenges for laser absorption spectroscopy systems at high pressures and achieved a sensor bandwidth of 100 kHz. The P(16) and R(6) transitions of the H<sub>2</sub>O fundamental antisymmetric stretch rovibrational band near 2.5 μm were chosen for initial development of this temperature diagnostic concept. Temperature validation experiments were conducted with shock tubes for both reactive and non-reactive environments. Shock tube experiments were first conducted with H<sub>2</sub>O and N<sub>2</sub> mixtures at pressures of around 8.2 atm, yielding temperature measurements with a standard deviation of 2.9 K within the steady-state test time. The performance of this system was then validated at 36.9 atm, yielding temperature measurements with a standard deviation of 8.4 K. By comparing the measured temperatures with calculated temperatures based on ideal shock jump relations, the sensor achieved an average accuracy within 4.3 K of the known temperatures across multiple experiments spanning a range of 1030–1450 K, 8–38 atm. These results demonstrate that the IMS-based sensor enables high-precision measurements of temperature at high pressures.

## 1 Introduction

Significant effort is currently directed toward developing high efficiency, low emission engines, especially those that can be operated at pressures higher than the current state of the art [1–3]. Unfortunately, due to the lack of experimental validation targets at these conditions, many state-of-the-art combustion models become invalid. Therefore, it is necessary to develop experimental diagnostics that can probe the physical and chemical nature of combusting fuels at high pressures to build more accurate numerical models [4–7].

Shock tubes are ideal facilities for studying high-temperature, high-pressure combustion phenomena as they can precisely control the initial thermodynamic conditions of a reactant mixture, most importantly the temperature and pressure [8–10]. Accurate knowledge of the temperature field is extremely important to studies of energy conversion systems

and reacting flows, particularly because temperature governs most key processes including heat/mass transport, reaction kinetics and fluid mechanics [11–13]. For example, when the heat release of the post-shock chemistry is non-negligible compared to the thermal mass of the gas mixture, temperature variation during the experimental test time is no longer insignificant and needs to be taken into consideration. At these conditions, the use of an accurate temperature sensor with short time response would help improve the quality of kinetics data.

Laser absorption spectroscopy (LAS) has been widely used to provide nonintrusive, in situ measurements of temperature, pressure, concentration, and velocity of target gas species for several decades [14–20]. Typical LAS techniques transmit the laser beam through the target gas sample at a wavelength corresponding to a specific absorption transition. By measuring the transmitted intensity and calculating absorbance, the thermodynamic properties of target gas species can be inferred. However, high-pressure LAS diagnostics are more challenging to develop compared with LAS diagnostics designed for low-pressure conditions. First, it is difficult or impossible to fully sweep a typical laser across an isolated absorption feature at high pressures due to pressure-induced lineshape broadening

---

Wei Wei and Wen Yu Peng contributed equally to this work.

✉ Wei Wei  
weiwei89@stanford.edu

<sup>1</sup> Department of Mechanical Engineering, Stanford University, Stanford, CA 94305, USA

and line overlap [21, 22]. Second, non-absorption transmission losses caused by density gradients along the optical path are magnified at high pressures and can significantly deteriorate the detection limit of optical sensors. Finally, other experimental noise sources such as low-frequency noise caused by vibrations and optical emission are often stronger at high pressures.

Among the variety of LAS techniques, wavelength modulation spectroscopy (WMS) is a well-known technique for addressing many of the aforementioned experimental difficulties and boosting the signal-to-noise ratio (SNR) [23–27]. WMS relies on modulating the laser wavelength at some high frequency  $f_m$  and detecting absorption at the modulation harmonics  $n \cdot f_m$ . By shifting the detection into a high-frequency domain, WMS is able to reject low-frequency additive noise and, with inter-harmonic normalization (e.g., the commonly used  $1f$ -normalization scheme), low-frequency multiplicative noise such as those induced by beam steering. However, WMS detection depends on the nonlinear interaction between laser wavelength and absorption curvature to introduce frequency content at the  $n > 1$  harmonics of the transmitted laser intensity signal, which usually requires the wavelength tuning range during each modulation cycle to be comparable to the absorption transition linewidth to achieve adequate signal strength. For typical single-mode semiconductor lasers, this constraint can be easily achieved at low pressures, but can be difficult at high pressures due to enhanced pressure broadening. As a result, WMS-based sensors for high-pressure environments must either operate with sub-optimal signal-to-noise ratios or with reduced modulation frequencies [28], resulting in limited applications for high-temperature and -pressure studies.

To overcome the high-pressure limitations of WMS while preserving the noise-rejection capabilities of WMS, a novel variant of the multi-color intensity modulation spectroscopy (IMS) sensing strategy was developed and demonstrated in this work. In IMS, only the laser intensity is modulated at some frequency,  $f_m$ , while the wavelength is fixed nominally at the peak of an absorption feature. This is achieved in practice with mechanical choppers, optical modulators [23, 29, 30], or through laser injection current modulation as used in this work. It is worth mentioning that injection current modulation inevitably introduces concurrent wavelength modulation, but this effect is usually negligible at the high-pressure conditions of interest in this study. Similar to the ubiquitous fixed-wavelength direct-absorption spectroscopy (fixed-DAS) technique, gas absorbance can be inferred from the transmitted IMS laser intensity by comparing the known incident  $1f$ -harmonic amplitude against the transmitted  $1f$ -harmonic amplitude.

Though the detection principles governing the IMS technique are similar to the fixed-DAS technique, several features distinguish the IMS technique used in this work from

fixed-DAS and enable the rejection of common experimental noise sources:

1. Since the first harmonic is used to measure gas absorption, low-frequency additive noise is automatically rejected from the IMS measurement through the lock-in filter operation similar to WMS.
2. Multiple wavelengths can be co-aligned and co-detected on the same detector by modulating the laser at distinct frequencies (known as frequency multiplexing) [31]. In addition to minimizing optical hardware complexity, the co-aligned and co-detected lasers can be used to mutually correct for multiplicative noise sources such as beam-steering losses and attenuation due to particulate matter occlusion. This is similar in principle to the inter-harmonic normalization scheme used in WMS to correct for bulk fluctuations in laser intensity.
3. Unlike WMS-based techniques and similar to fixed-DAS diagnostics, there are no penalties in terms of detection signal strength for modulating the laser intensity at arbitrarily high frequencies using the IMS strategy. This enables very high measurement bandwidths and allows for the diagnostic to be used in high-pressure environments in a similar fashion as fixed-DAS sensors used in numerous prior publications using high-pressure shock tube facilities (see Shao et al. [32] for a recent example).

Overall, these three features blend the noise-rejection capabilities of WMS together with the high-bandwidth and high-pressure capabilities of traditional fixed-DAS sensing. These capabilities were demonstrated in this work with a two-color IMS-based sensor designed to perform high-bandwidth measurements of temperature in high-pressure shock tube environments. Specifically, the sensor uses two co-aligned frequency-multiplexed tunable diode lasers (TDLs) targeting mid-infrared  $\text{H}_2\text{O}$  transitions near  $4029.5 \text{ cm}^{-1}$  (2482 nm, P(16) transition) and  $3920.1 \text{ cm}^{-1}$  (2551 nm, R(6) transition) to infer temperature. Sensor validation was conducted with shock-heated mixtures of  $\text{H}_2\text{O}$  diluted in  $\text{N}_2$  at temperatures between 1030 and 1450 K and pressures between 8 and 38 atm. The results of the IMS sensor validation experiments demonstrated high measurement precision. Additionally, although previous researchers have demonstrated accurate measurements of temperature and  $\text{H}_2\text{O}$  mole fraction at pressure up to 50 atm using similar absorption transition pairs with the WMS- $2f/1f$  strategy [28], the 100 kHz sensor bandwidth achieved with this IMS-based sensor opens the opportunity to perform measurements at rates that are no longer limited by the wavelength tuning range requirements of WMS.

To the authors' knowledge, this work represents the first demonstration of an IMS-based sensing strategy that incorporates the noise-rejection features commonly found

in WMS-based sensors while also being able to operate at high pressures and measurement rates without compromising detection signal strength. Further extensions of this measurement strategy can generalize this measurement strategy to greater pressures (e.g., practical combustion engines) and measured quantities (e.g., simultaneous speciation and thermometry). These extensions are discussed in Sect. 5.4.

## 2 Principles

### 2.1 Laser absorption spectroscopy

Absorption spectroscopy theory is briefly outlined here to clarify the notation. The Beer–Lambert law provides the physical relation governing narrow-band laser absorption spectroscopy. The equation relates the incident light intensity  $I_0$  and transmitted light intensity  $I_t$  through a gas medium by:

$$-\ln\left(\frac{I_t}{I_0}\right) = \alpha_\nu = \sum_i S_i(T)\phi_i(\nu)L P X_{abs}, \quad (1)$$

where  $I_t/I_0$  is the ratio of transmitted light intensity to incident light intensity.  $S_i$  ( $\text{cm}^{-1}\text{atm}^{-1}$ ) is the temperature-dependent transition linestrength of transition  $i$ ,  $\phi_i(\nu)$  ( $\text{cm}$ ) is the wavelength-dependent lineshape function,  $L$  ( $\text{cm}$ ) is optical path length,  $P$  ( $\text{atm}$ ) is the total pressure of the gas and  $X_{abs}$  is the mole fraction of absorbing species.  $\phi_i(\nu)$  can be well approximated by the Voigt function in most cases, which models the combined effects of collisional broadening and Doppler broadening, characterized by their respective full-width at half-maximum (FWHM),  $\Delta\nu_C$  ( $\text{cm}^{-1}$ ) and  $\Delta\nu_D$  ( $\text{cm}^{-1}$ ). The collisional FWHM is modeled as:

$$\Delta\nu_C = P \sum_A X_A 2\gamma_{H_2O-A}, \quad (2)$$

where the subscript A stands for all species within the gas mixture and  $\gamma_{H_2O-A}$  ( $\text{cm}^{-1}\text{atm}^{-1}$ ) is the collisional broadening coefficient for  $H_2O$  with species A. The variation of the broadening coefficient  $2\gamma$  with temperature can be approximated as:

$$2\gamma(T) = 2\gamma(T_0)\left(\frac{T_0}{T}\right)^N, \quad (3)$$

where  $T$  ( $K$ ) is the temperature,  $T_0$  ( $K$ ) is some reference temperature (296 K is used here and for most spectroscopic databases).  $N$  is the temperature coefficient for collisional broadening.

The Doppler FWHM is given as:

$$\Delta\nu_D = \nu_0(7.1623 \times 10^{-7})\left(\frac{T}{M}\right)^{0.5} \quad (4)$$

where  $\nu_0$  ( $\text{cm}^{-1}$ ) is the transition center frequency,  $M$  is molecular weight ( $\text{g/mol}$ , 18.015  $\text{g/mol}$  for  $H_2O$ ).

For molecules with small molecular weight and large rotational energy level spacing, such as  $H_2O$ , HF, HCN, etc., collisional narrowing needs to be considered for accurate lineshape models [33–36]. If pronounced collisional narrowing cannot be neglected, then either the Galatry [37] or Rautian [38] profiles can be used to better describe the absorption lineshape. An additional parameter is used to account collisional narrowing:

$$\nu_{VC} = P \sum_A X_A \beta_A(T), \quad (5)$$

where  $\nu_{VC}$  ( $\text{cm}^{-1}$ ) represents the effective frequency at which a molecule's velocity is randomized by collision.  $\beta_A$  ( $\text{cm}^{-1}/\text{atm}$ ) is the collisional narrowing coefficient. Variation of the collisional narrowing coefficient  $\beta_A$  with temperature can be approximated as:

$$\beta(T) = \beta(T_0)\left(\frac{T_0}{T}\right)^n, \quad (6)$$

where  $n$  is the temperature coefficient for collisional narrowing.

### 2.2 Intensity modulation spectroscopy

In IMS, the laser intensity is modulated sinusoidally at frequency  $f_m$  typically with mechanical choppers, electro-optic modulators, or injection current tuning. The instantaneous intensity modulation (IM) waveform can be described as a general Fourier series:

$$I_0(t) = \bar{I}_0 \cdot \left[ 1 + \sum_{k=1}^{\infty} i_k \cos(2\pi k f_m t + \varphi_k) \right], \quad (7)$$

where  $\bar{I}_0$  is the average laser intensity, and  $i_k$  are the normalized linear ( $i_1$ ) and nonlinear ( $i_2, i_3, i_4 \dots$ ) IM amplitudes.  $\varphi_k$  are the temporal phases between modulation control and IM. For maximum accuracy,  $\bar{I}_0$ ,  $i_k$  and  $\varphi_k$  are directly measured with a photovoltaic detector prior to the experiment. For sinusoidal intensity modulation as used in this work,  $i_1$  is in general much greater than  $i_{k>1}$ . Unlike in WMS-based sensors, the optical frequency of the laser is kept at some constant,  $\nu_0$  ( $\text{cm}^{-1}$ ) or kept sufficiently small in range such that the gas absorbance is nearly constant at some value,  $\alpha_0$ . With this simplification, the transmitted intensity can be expressed simply as follows:

$$I_t(t) = \eta(t)I_0(t) \cdot \exp(-\alpha_0) + \rho(t). \quad (8)$$

Here,  $\eta(t)$  and  $\rho(t)$  are multiplicative (e.g., due to non-absorption transmission losses such as beam steering and particulate matter occlusion) and additive (e.g., due to optical emission or noise in the detection electronics) noise. Assuming that the frequency bandwidths of  $\rho(t)$  and  $\eta(t)$  are significantly less than  $f_m$ , it is possible to isolate the amplitude of the first harmonic of the transmitted intensity,  $S_{1f,t}(t)$ , via lock-in filters to yield an expression that is independent of low-frequency additive noise originating from the experimental environment:

$$S_{1f,t}(t) = G\eta(t)\overline{I_0}i_1 \cdot \exp(-\alpha_0), \quad (9)$$

where  $G$  is the electro-optical gain of the photodetector. With knowledge of  $\overline{I_0}$  and  $i_1$  known from the pre-experiment characterization, it is possible to infer  $\alpha_0$  from  $S_{1f,t}(t)$  assuming that the non-absorption transmission losses are negligible (e.g.,  $\eta(t) \approx 1$ ).  $\alpha_0$  can then be used to infer the gas parameters based on known spectroscopic models of the absorbing gas species described in Sect. 2.1. Unlike some WMS-based sensors, background subtraction is not needed for this sensor.

### 2.3 Two-color co-aligned IMS

For environments where non-absorbing transmission losses are not negligible (e.g., in transient high-pressure environments such as the shock tubes studied in this work), it is desirable to remove or correct the dependence of  $S_{1f,t}(t)$  on  $G\eta(t)$ . This can be accomplished through the co-alignment and co-detection of multiple lasers probing different absorption transitions of the same species. Individual contributions from each laser to the transmitted intensity can be isolated by modulating each laser at different IM frequencies. Assuming that the co-propagating beams are perfectly co-aligned and co-detected,  $G\eta(t)$  experienced by each beam across the absorbing medium will be identical as long as the wavelengths are relatively similar. This allows for the cross-normalization of  $S_{1f,t}(t)$  for distinct wavelength pairs to construct a ratio,  $R$ , that is independent of  $G\eta(t)$  as follows:

$$R = \frac{\overline{I_{0,a}}i_{1,a}}{\overline{I_{0,b}}i_{1,b}} \cdot \exp[-(\sigma_a(T) - \sigma_b(T))PXL]. \quad (10)$$

Here, the subscripts  $a$  and  $b$  denote the two laser wavelengths.  $\sigma_a(T)$  and  $\sigma_b(T)$  represent the temperature-dependent pressure-normalized absorption cross sections of the gas at the two wavelengths, which may be expressed for arbitrary optical frequencies,  $\nu^*$ , as  $\sigma_{\nu^*}(T) = \sum_i S_i(T)\phi_i(\nu = \nu^*)$ . These cross sections are either well known from spectroscopic models of the absorbing species or can be experimentally measured.

With  $P$ ,  $X$ , laser properties ( $I_0(t)$ ,  $\nu_0$ ,  $i_k$ ), and  $L$  known, it is possible to infer the temperature of the absorbing gas from  $R$  assuming that the absorption cross sections of the two probed wavelengths vary distinctly as a function of temperature. In the context of isolated absorption transitions, this constraint is identical to the need for the lower-state energies of the two absorption transitions to be significantly different to enable sensitive detection of temperature.

It is useful to clarify precisely what the authors imply by “relative similarity” in wavelength for the non-absorbing transmission losses ( $\eta(t)$ ) normalization to succeed. This is important because absorption cross sections of nearby wavelength pairs have generally similar temperature dependences for high-pressure or large-molecule gases with heavily blended and featureless absorption spectra. Thus, for thermometry applications, it is beneficial to choose wavelength pairs that probe distinct regions of an absorption band to maximize temperature sensitivity. Unfortunately, this constraint may result in deviations in  $\eta(t)$  between the two wavelengths due to refractive index  $n$  dispersion within the beam path, resulting in an imperfect correction. However, refractive indices are generally very weak functions of wavelength in gases. For example, for dry air at room temperature and 1 atm,  $n - 1$  at 2.5 and 2.8  $\mu\text{m}$  differ by only 0.04 % [39] demonstrating that refractive indices do not change significantly across a significant portion of the  $\text{H}_2\text{O}$  absorption band near 2.64  $\mu\text{m}$ . This allows for the selection of distinct wavelength pairs within a molecular absorption band while maintaining adequate similarity in refractive indices.

## 3 Sensor design

### 3.1 Transition selection

Choosing appropriate species and target absorption transitions is vitally important for the performance of TDLAS diagnostic systems. Water was chosen for this temperature diagnostic due to its ubiquity in combustion-relevant shock tube environments and the distinctness of its molecular spectra. Simulated spectra based on the HITEMP database [40] were used to identify the most appropriate transitions. After careful consideration, the P(16) and R(6) transitions near 4029.5 and 3920.1  $\text{cm}^{-1}$ , respectively, of the fundamental asymmetric stretch vibration band were selected for the following reasons:

- (1) *Strong absorbance* Figure 1a, b shows simulated absorbance spectra for these lines at 1300 K, 10 atm, 2 %  $\text{H}_2\text{O}$  by mole fraction with a path length of 10 cm. Peak absorbances are around 0.2, which is well within the desired absorbance bounds between 0.01 and 1.5 for typical LAS sensors.

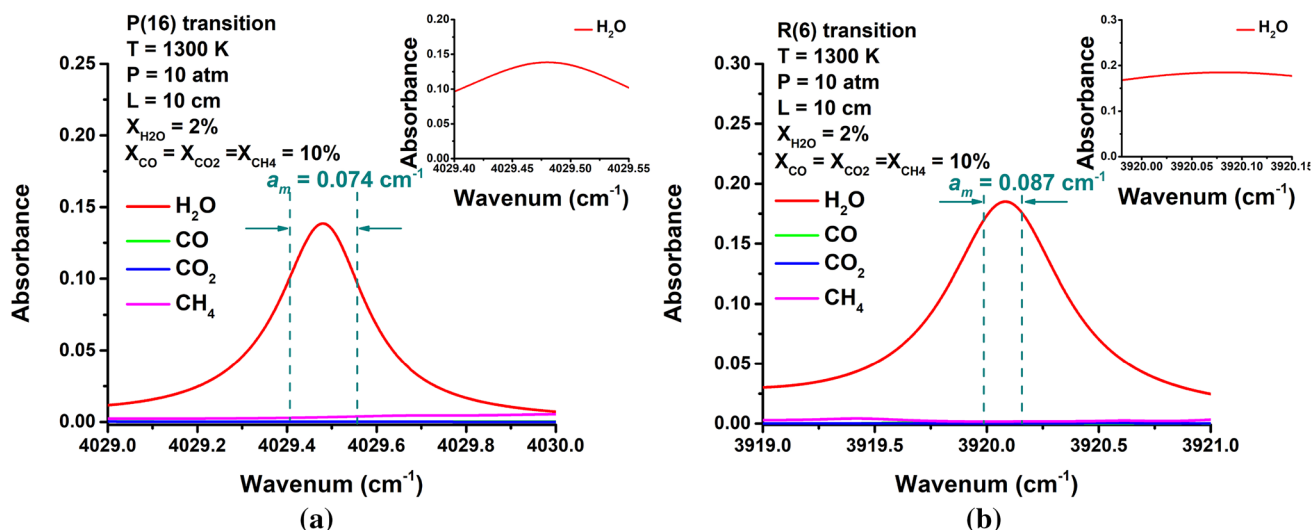


**Fig. 1** **a** Simulated absorbance spectra for the P(16) transition at temperature of 1300 K, pressure of 10 atm, optical length of 10 cm and H<sub>2</sub>O mole fraction of 2%. Scan range of the P(16) transition laser

is shown with vertical dashed lines. **b** simulated absorbance spectra for the R(6) transition at the same conditions. Scan range of the R(6) transition laser is shown with vertical dashed lines

(2) Minimal spectral interference. The absorbance spectra of common combustion species including CO, CO<sub>2</sub>, CH<sub>4</sub> with mole fraction of 10% are shown in Fig. 1a, b. Absorbance interferences are less than 2% of the peak H<sub>2</sub>O value despite interfering species mole fractions that are five times larger than the H<sub>2</sub>O mole fraction. It is worth mentioning that although the two H<sub>2</sub>O transitions used in this work were selected to be minimally sensitive to interference from other species, IMS signals are nonetheless sensitive to broadband spectral interference unlike WMS-based sensing strategies. This places a limit on the utility of an IMS diagnostic at high temperatures and pressures due to the strengthened spectral interference from competing species. In such environments, the use of additional laser wavelengths such as the on- and off-line detection strategy described in Sur et al. [41] can help decouple the contributions to the overall absorption at each wavelength from interfering species.

### 3.2 Optimization of laser tuning parameters

The criteria for optimizing the laser tuning parameters of a two-color IMS sensor are relatively straightforward:

1. To maximize the signal strength of  $S_{1f,t}$  (Eq. 9), the IM amplitude ( $i_1$  in Eq. 7) of each laser should be set as high as possible (e.g., as close to 1 as possible). For injection current-modulated lasers as used in this work, this is equivalent to setting the injection current waveform to tune between the threshold and saturation currents during each modulation cycle.

2. To maximize noise rejection via the lock-in filter operation, modulation frequencies for the two lasers should be set as high as possible. Due to laser controller hardware limitations for this sensor,  $f_m$  was limited to 1 MHz.
3. The modulation frequencies of the two lasers should be set such that the difference in modulation frequencies,  $|f_b - f_a|$ , between the two lasers is equal to twice the desired sensor bandwidth. For this sensor to achieve a 100 kHz bandwidth (sufficient to resolve transient phenomena associated with most combustion reactions studied in shock tubes), the lasers probing the P(16) and R(6) transitions were modulated at 800 kHz and 1 MHz, respectively.

As noted previously, the lasers in this work were modulated using injection current tuning to minimize hardware complexity relative to other intensity modulation methods (e.g., there is no need for dedicated mechanical choppers or optical modulators). However, as a side effect of injection current tuning, the laser also tunes across some range of wavelengths (referred to as the modulation depth and denoted as  $a_m$ ) during each modulation cycle due to ohmic heating. Figure 2 shows the linear IM amplitude  $i_1$  and modulation depth as functions of modulation frequency for the two lasers used in this work. An etalon with FSR of 0.0161 cm<sup>-1</sup> and a data acquisition (DAQ) with sampling rate of 80 MS/s were used to characterize the lasers. As can be seen, the P(16) and R(6) lasers tune across a range of 0.074 and 0.087 cm<sup>-1</sup>, respectively, at their operating modulation frequencies. For very high-pressure gases or for heavily blended spectral regions, this modulation depth is inconsequential to the IMS framework discussed in Sect. 2.2 since the constant-absorbance



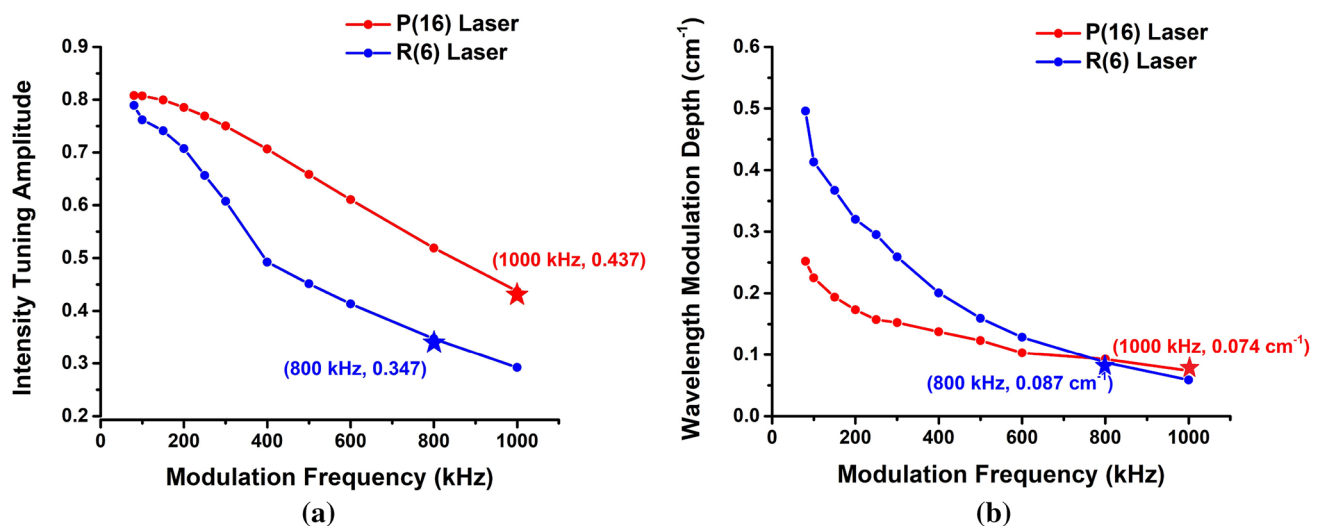


**Fig. 2** Variation of the laser linear intensity tuning amplitude  $i_1$  (a) and modulation depth  $a_m$  (b) as functions of modulation frequency at the maximum allowable injection current amplitude

assumption is valid. However, for the discrete H<sub>2</sub>O spectral features probed here, the modulation depths of the two lasers are somewhat comparable to the width of the absorption features as shown with the teal-dotted lines in Fig. 1 at the relatively low pressure of 10 atm shown here. Since  $\alpha$  is not constant across the range of wavelengths at these low pressures, Eq. (9) is not a valid expression for the first harmonic magnitude. For these conditions, the simulation strategy in Sun et al. [42] can be used to account for lineshape effects when calculating  $S_{1f,t}$ . Though this complicates the expressions for Eqs. 9 and 10 and requires some knowledge of absorption lineshape, the procedures for determining temperature are still valid.

## 4 Thermometry demonstrations

### 4.1 Experimental setup

Validation experiments were performed in the flexible applications shock tube (FAST) and the high-pressure shock tube (HPST) facilities at the Stanford High- Temperature Gasdynamics Laboratory. The FAST facility has a circular cross section with an inner diameter of 13.97 cm with wedged sapphire optical access ports located 1 cm from the end wall. The HPST facility has a circular cross section with an inner diameter of 5.0 cm and sapphire optical access ports located 1.1 cm from the end wall. Thorough discussions of the FAST [43] and HPST facilities [44, 45] can be found in previous studies.

The optical setup was nearly identical for the two shock tubes and is shown with a computer rendering in Fig. 3. Co-alignment was accomplished using a pair of kinematically

adjustable turning mirrors for each laser and a 50/50 CaF<sub>2</sub> beamsplitter (all from Thorlabs, Inc.). The turning mirrors were adjusted until the beams co-propagated through a pair of irises placed downstream of the beamsplitter. The irises were also sufficiently constricted to ensure the light from the two lasers had nearly identical beam propagation vectors through the shock tube. A  $f = 15$  cm off-axis parabolic mirror was placed downstream of the second iris to focus the co-propagating beams on the center of the shock tube. With reflected shock speeds typically in the order of 500 m/s and average beam diameter of 1 mm, the effective temporal resolution of the optics was 2  $\mu$ s. The transmitted intensity was focused onto a photodetector (PDA10D InGaAs Fixed Gain Amplified Detector, Thorlabs) with a  $f = 20$  mm CaF<sub>2</sub> focusing lens and a 15 MHz detection bandwidth. It should be noted that the optical system was constructed with optical cage mounts, which allowed for simple, robust alignment procedures and an overall assembly that can be easily transported and integrated onto arbitrary test environments.

The two lasers used to probe water transitions were two distributed feedback diode lasers (DFB-DLs, Nanoplus). Intensity modulation was achieved through varying the injection current produced by a commercial laser driver (ILX Lightwave LDX- 3232). The lasers were frequency-domain multiplexed [46] and digital lock-in amplifiers (LIA) with 100 kHz bandwidth were used to separate the modulated signals of each laser from the same detector signal based on the modulation frequency.

During each shock tube experiment, the test section was filled with low-pressure test gas (with temperature and pressure denoted as T1 and P1, respectively) and was instantaneously and homogeneously heated to high temperatures and pressures (denoted as T5 and P5, respectively), by an

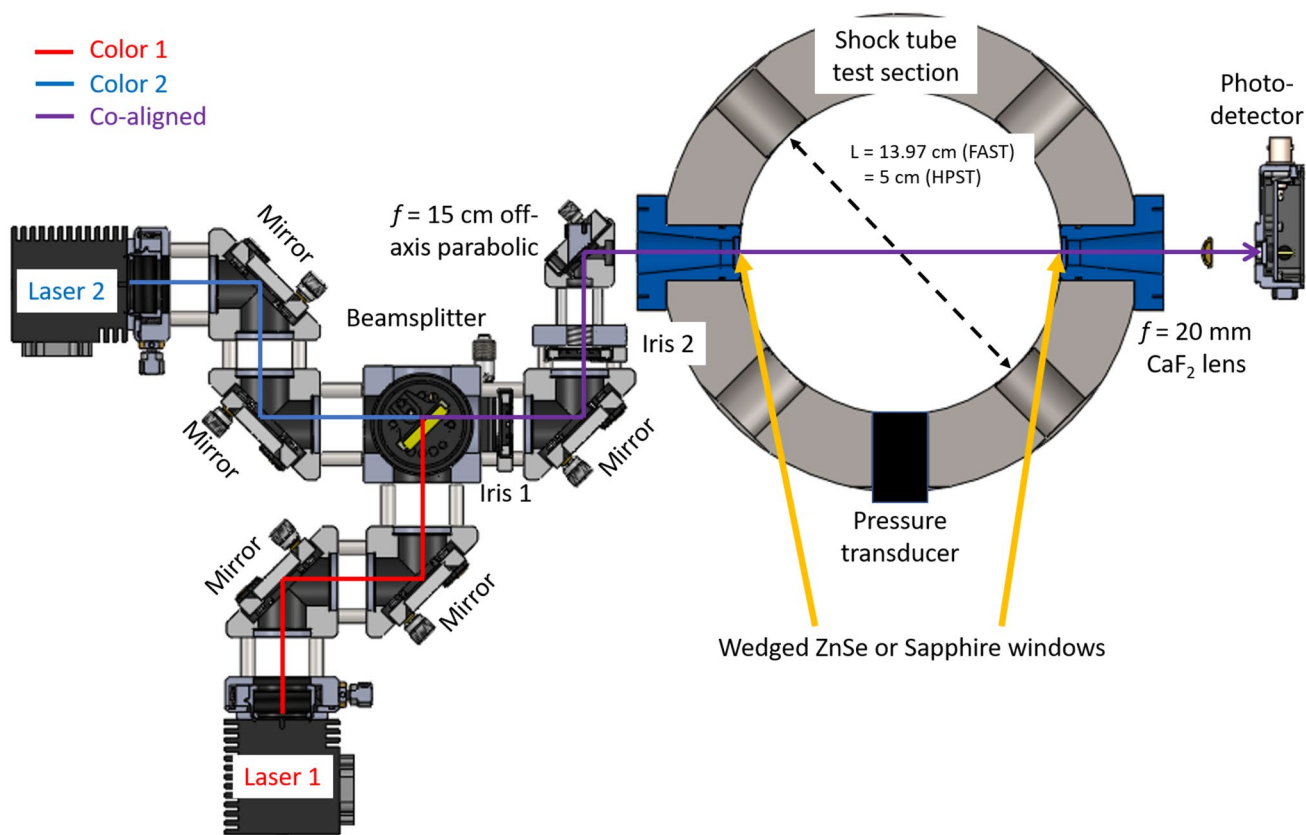


**Fig. 3** Computer rendering of the experimental setup used for two-color IMS temperature measurements in the shock tubes. Key elements of the laser co-alignment and launching optics and optical

paths are labeled. Color 1 represents the light targeting the P(16) transition, while color 2 represents the light targeting the R(6) transition

incident and reflected shock wave pair. Gas pressure was monitored by Kistler 603B1 pressure gauges axially co-located with the probing light beams for both shock tubes. Initial post-reflected shock temperatures and pressures can be determined using the known test gas composition, the incident shock velocity at the end wall as measured by five piezoelectric pressure transducers axially distributed along the shock tubes, and the FROSH shock-jump thermodynamics solver [47]. Due to pressure rise within the test time during each experiment caused by non-ideal shock attenuation effects, the temperature time history after the passing of the reflected shock was simulated based on the pressure time history assuming constant entropy.

## 4.2 FAST facility experiments

This temperature diagnostic system was first validated at lower pressures (around 8 atm) in the Stanford FAST facility for non-reacting  $\text{H}_2\text{O}/\text{N}_2$  mixtures. Due to the non-negligible modulation depths of the two lasers at these pressures, the absorption lineshapes throughout the optical frequency modulation were simulated to maximize accuracy. Voigt

and Galatry profiles were used to model the R(6) and P(16) transitions using spectroscopic parameters from Goldenstein et al. [48, 49]. Without the lineshape models to account for the non-constant absorbance during each modulation cycle, simulations suggest that the temperature measurements would deviate from known values by 15 K at reflected shock conditions of 1300 K and 8 atm. Figure 4a shows a representative two-color IMS measurement in a 2 %  $\text{H}_2\text{O}/\text{N}_2$  balance test gas mixture by mole at initial reflected shock conditions of 1134 K and 8.2 atm. The raw detector signal is shown in red and the test section pressure time history is shown in blue. The laser intensity in the period immediately after the arrival of the reflected shock is magnified with an inset figure. The bulk changes in the measured intensity near the incident and reflected shock arrivals were caused by multiple factors including a change in absorption strength due to shock-induced temperature jump (especially for the P(16) transition), lineshape broadening due to the pressure jump, and attenuation due to beam steering. The detector signal drift during the test time was caused by thermal emission by  $\text{H}_2\text{O}$  and other impurities. Figure 4b shows the individual demodulated first-harmonic signals ( $S_{1f,t}$  in Eq. 9) for the

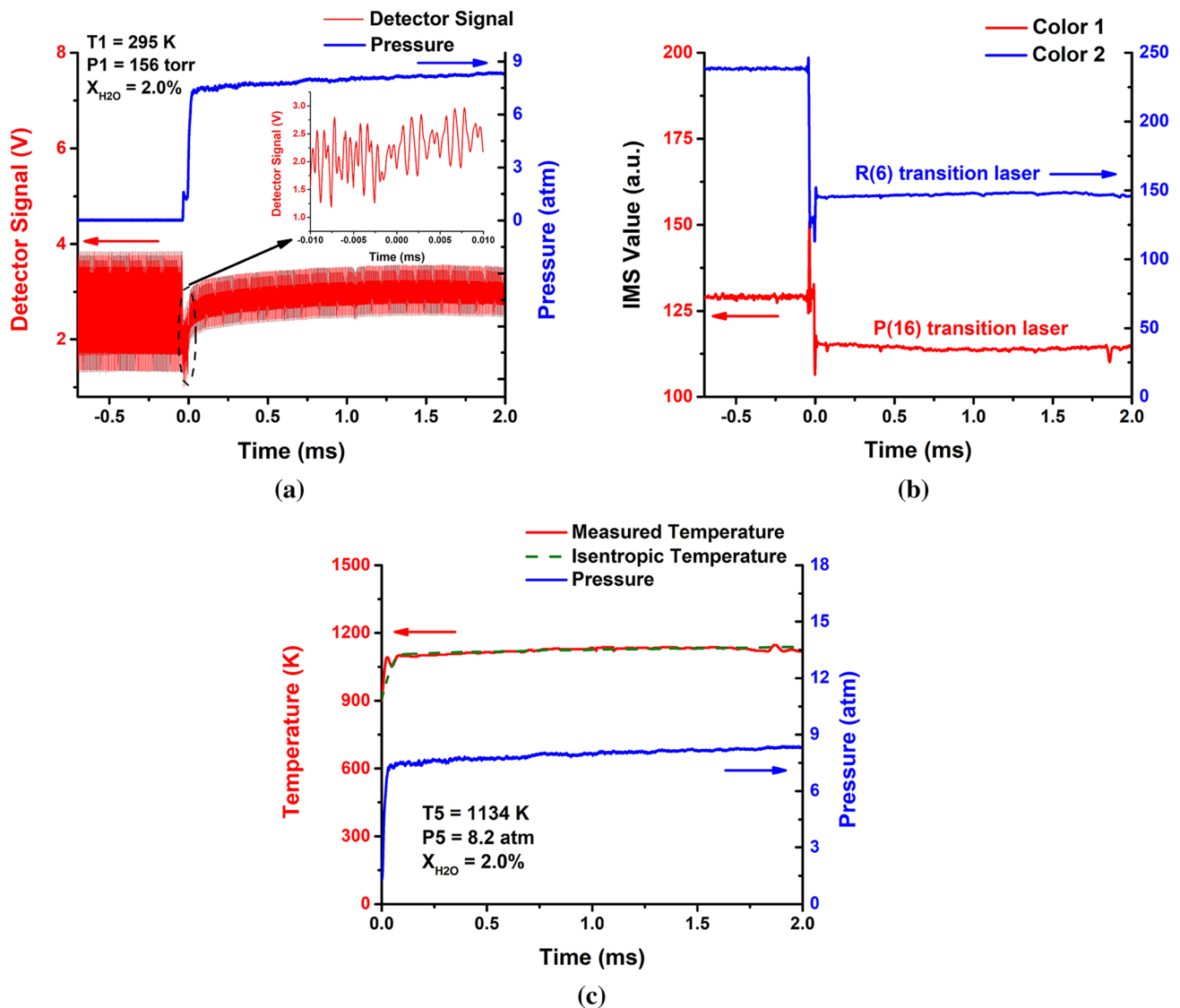


**Fig. 4** **a** Transmitted laser intensity (red) and pressure trace (blue) during a shock tube experiment at initial post-reflected shock pressure of 8.2 atm. The inset highlights the dynamics of the raw detector sig-

nal during the passing of the reflected shock. **b** Measured IMS signal values for the two lasers. **c** Measured temperature (red) compared against calculated temperature (green dotted)

two lasers. Assuming a known  $\text{H}_2\text{O}$  mole fraction based on pre-shock manometric measurements of the test gas, the IMS signal ratio (Eq. 10) can be used to determine the temperature as discussed in Sect. 2.3.  $\text{H}_2\text{O}$  wall adsorption was minimized by reducing the time delay between test gas loading and the shock experiment. By monitoring the WMS- $2f/1f$  magnitude of the R(6) transition prior to each shock, it was possible to verify that the water concentration has not changed significantly relative to the manometrically prepared value. Measurements within the post-reflected shock test time are shown in Fig. 4c, which contains the measured temperature time history (red line) and the calculated isentropic temperature time history (green dotted line) based on the measured pressure time history (blue line).

Assuming the isentropic, chemically inert conditions during shock tube test time (about 2 ms), the standard deviation of measured temperature time history ( $T_{\text{meas}}(t)$ ) relative to the isentropic temperature time history ( $T_s(t)$ ), defined here as  $\sigma_T = \text{std}(T_{\text{meas}}(t) - T_s(t))$ , was calculated to be 2.9 K, which corresponds to a  $1 - \sigma$  precision of only 0.26 % relative to the initial post-shock temperature of 1134 K.

### 4.3 HPST facility experiments

The performance of this temperature diagnostic was further demonstrated at much higher pressures (around 38 atm) using the HPST facility. As discussed previously, the modulation depths of the lasers relative to the FWHM of the



target absorption transitions are sufficiently low at such high pressures ( $2a_m/FWHM = 0.0438$  and  $0.0191$  for the P(16) and R(6) lasers, respectively, at 1300 K, 37 atm) that the absorption spectrum can be treated as approximately constant throughout the laser scans, simplifying the analysis to the IMS framework discussed in Sect. 2.2. This simplification eliminates certain uncertainties from the measurement framework such as uncertainties in the mean laser wavelength.

The shock tube test gas was composed of 3.7% H<sub>2</sub>O by mole diluted in N<sub>2</sub>. Figure 5a shows a representative data trace at the initial reflected shock conditions of 1316 K, 36.9 atm. An identical set of LIA parameters used for the FAST experiments converted detector signal into IMS signals, which were subsequently used to infer the temperature time history shown in Fig. 5b in red lines. Again, assuming nonreacting isentropic changes in thermodynamic conditions during the shock tube test time (0.6 ms), the standard deviation of measured temperature relative to the isentropic temperature time history was calculated to be 8.4 K, which corresponds to a  $1 - \sigma$  precision of only 0.64% relative to the initial post-shock temperature of 1316 K.

Similar validation measurements were repeated in both FAST and HPST facilities at pressures around 8 and 38 atm, respectively. Figure 6 summarizes the accuracy of this temperature diagnostic by plotting the average measured temperature during each experimental test time against known average temperature calculated based on ideal shock relations and assuming post-shock isentropic

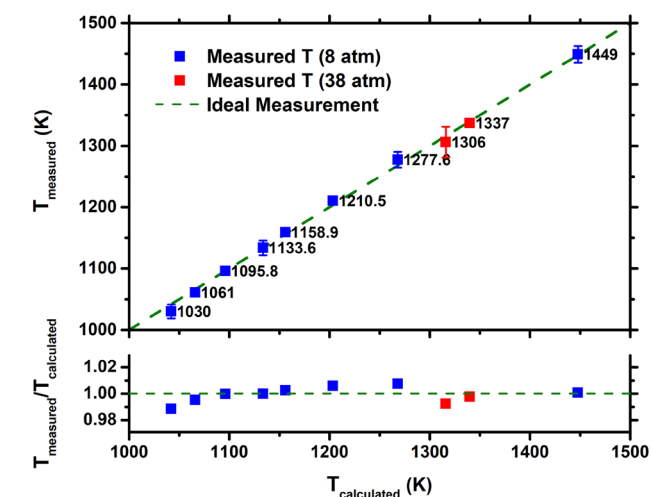
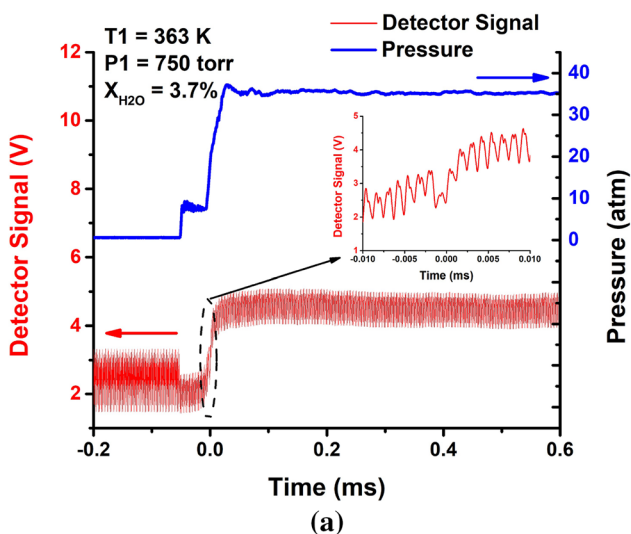


Fig. 6 Test time-averaged measured temperatures in the FAST facility (blue dots) and HPST facility (red dots) plotted against calculated average temperatures using ideal shock relations and isentropic relations. The green dashed line stands for ideal measurement when measured temperatures are equal to calculated temperatures. Error bars represent  $1 - \sigma$  precisions of the measurements, some of which are too small to see in the figure

changes in conditions during the test time. Throughout the experiments, the measured temperatures stayed within 0.6% of the calculated temperatures over the 1030–1450 K range with an average  $1 - \sigma$  precision of only 4.3 K. These results demonstrate that the IMS-based sensor used in this work enables high-precision measurements of temperature at high pressures.

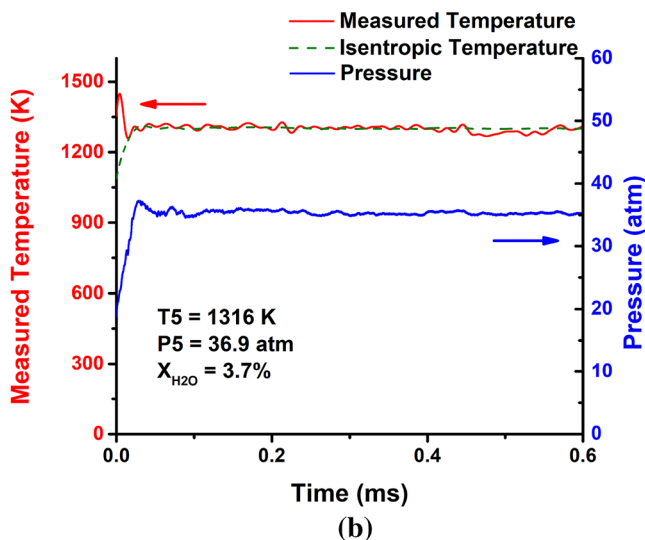


Fig. 5 a Transmitted laser intensity (red) and pressure trace (blue) during a shock tube experiment at initial post-reflected shock pressure of 36.9 atm. The inset highlights the dynamics of the raw detector sig-

nal during the passing of the reflected shock. b Measured temperature (red) compared against calculated temperature time history based on shock jump isentropic compression (green dashed)

#### 4.4 Uncertainty analysis

Uncertainty analysis was performed to assess the accuracy of the IMS-based temperature sensor. Primary sources of uncertainty include fluctuations in the mean laser wavelengths, uncertainty in the spectroscopic parameters of the targeted absorption transitions and its surrounding contributors, and uncertainty in the precise concentration of water loaded into the shock tube prior to each experiment. Each source of uncertainty was assigned Gaussian probability distributions with mean and standard deviation equal to their reported mean values and uncertainties (e.g., based on uncertainty codes reported for each spectroscopic parameter or manufacturer-stated uncertainties for pressure transducers used to prepare mixtures). Monte Carlo simulations of these parameter distributions were used to generate a distribution of possible temperatures as measured by the IMS sensor. The standard deviation of the resulting temperature distribution (also Gaussian in shape) was reported as the uncertainty in temperature for a given shock tube experiment.

For conditions near 8 atm as measured in the FAST, temperature uncertainty was calculated to be  $\pm 12$  K on average and is primarily driven by laser center wavelength and water loading uncertainties, which contributed on average 2.76 K and 2.16 K, respectively, to the overall uncertainty. Measurement uncertainty for HPST experiments near 38 atm was  $\pm 25$  K on average, larger than the uncertainty at lower pressures. Here, uncertainties in laser wavelength were inconsequential due to the heavily broadened spectra at the targeted wavelengths. However, uncertainties in spectroscopic parameters for the targeted absorption transitions and their neighbors were the dominant contributors to the measurement uncertainty. In particular, collisional broadening and linecenter shift parameter uncertainties were found to be responsible for 6.5 K and 5.25 K of the total uncertainty, respectively. Although this sensor has been validated up to pressures of 38 atm, the sensor, in principle, can be reliably operated at significantly greater pressures. Specific operability pressure limits are heavily facility dependent and difficult to determine without additional high-pressure data. However, we envision that the key limiting factors for the effectiveness of this sensor at extreme pressures include unacceptably high uncertainties in the absorption model, enhanced non-absorbing transmission losses, and a loss of temperature sensitivity between the two target wavelengths due to the blending of neighboring absorption transitions.

To provide meaningful bounds for the upper pressure limit of this IMS shock tube thermometry sensor, we note that Almodovar [50] successfully measured the absorption cross section of nitric oxide at pressures up to 112 atm with a fixed-DAS diagnostic. Given that the theoretical bases of IMS and fixed-DAS are nearly indistinct, it is not difficult to envision the usability of the current IMS sensor at these

pressures provided that the spectroscopic models for water at the target wavelengths are sufficiently well characterized.

With regard to the loss of temperature sensitivity between the two target wavelengths, HITEMP simulations at 1300 K suggest that the targeted absorption transitions (R(6) and P(16) near  $4029.5\text{ cm}^{-1}$  and  $3920.1\text{ cm}^{-1}$ , respectively) contribute greater than 50% of the total absorbance at their respective wavelengths at pressures up to 80 atm. Therefore, the sensitivity of the IMS signal ratio to temperature for these two transitions largely tracks what is expected based on the difference in lower state energies between the two absorption transitions up to 80 atm.

Overall, this analysis illustrates specific needs for minimizing two-color IMS thermometry measurement uncertainty at various pressure regimes. For relatively low pressures where absorption spectra are discrete and well characterized, laser wavelengths should be monitored regularly with wavemeters or reference gas cells. For extreme pressures, though laser wavelength uncertainty minimally impacts measurement accuracy due to enhanced spectral broadening, uncertainty in absorption cross sections becomes the dominant source of error, especially as high-pressure effects such as line mixing and spectral blending across multiple absorption transitions become non-negligible. In such applications, it is useful to build high-temperature and high-pressure spectral databases such as those found in [51–53] to minimize measurement uncertainties.

## 5 Additional advantages and extensions

As noted in Sects. 2.2 and 2.3, the detection principles underlying the two-color IMS sensing technique can be interpreted as “enhancements” to conventional fixed-wavelength direct-absorption spectroscopy (fixed-DAS) techniques. Key enhancements include the ability to reject additive noise and non-absorption losses, both of which are beneficial characteristics shared with WMS-based techniques. Also, unlike WMS and similar to fixed-DAS sensors, IMS sensor measurement rates can be arbitrarily high without compromising measurement fidelity since the technique is only sensitive to the absolute absorbance. These distinctions are experimentally demonstrated and discussed in this section. Additionally, several extensions intended to improve the performance and capabilities of the IMS-based sensor used in this work are identified and described.

### 5.1 Desensitization to non-absorption losses with co-aligned cross-normalization

We now demonstrate the two-color IMS sensor’s ability to reject non-absorption losses. For the high-pressure shock tube environments studied in this work, LAS sensors are

typically subjected to losses induced by strong density gradients and particulate matter occlusion from shattered diaphragm pieces. These effects are further exacerbated by the small-aperture windows designed to survive high pressures, requiring narrow beams and precision alignment that significantly challenge the performance of LAS systems. The sensor presented in this work alleviates some of these challenges through the use of two-color cross-normalization as discussed in Sect. 2.3.

Figure 7 shows data traces for a two-color IMS measurement in a 2%  $\text{H}_2\text{O}/\text{N}_2$  balanced test gas at reflected shock conditions of 1043 K, 7.7 atm. It can be seen near  $t = 2.2$  ms that a plastic diaphragm fragment intercepted and occluded part of the optical path, resulting in a sharp decrease in the photodetector and demodulated IMS signals as outlined in dotted orange boxes in Fig. 7a, b. These events are common in shock tube experiments and typically require the experimentalist to remove these spurious data points in post-processing. However, as shown in Fig. 7b using the cross-normalization scheme, the occlusion-induced fluctuation in the inferred temperature was only 9.6% relative to the initial post-shock temperature of 1042 K as compared to 28% if using the only the raw IMS signal of the R(6) absorption transition near  $3920.1\text{ cm}^{-1}$ .

It should be noted that, due to the imperfect free-space co-alignment of the two lasers used in this work, the IMS cross-normalization scheme is not as successful at removing non-absorption losses from the measurement as WMS- $n/f/1f$  techniques. For example, for the same measurement shown in Fig. 7, the WMS- $2f/1f$  signal for the P(16) absorption

transition saw only a 2.5% amplitude fluctuation during the passage of the diaphragm fragment. However, if the same diaphragm piece were to occlude the beam path at HPST-relevant pressures near 37 atm, the WMS- $2f/1f$  signal would fluctuate at 32% relative to its nominal value due to the weakening of the  $2f$  signal from enhanced lineshape broadening at elevated pressures. Additionally, better co-alignment strategies such as coupling multiple lasers into a single-mode optical fiber would yield significant improvements to the two-color IMS cross-normalization scheme. With these improvements, it is expected that the IMS cross-normalization scheme would rival the non-absorbing loss rejection capabilities of  $1f$ -normalization.

## 5.2 Low-frequency additive noise rejection

Typical direct-absorption LAS systems experience low-frequency additive noise as measured by the photodetector, deteriorating detection sensitivity if not adequately mitigated. Among the various low-frequency noise sources in combustion-relevant high-pressure environments, broadband thermal emission is generally the strongest. Spectral filters are commonly used to suppress thermal emission, but unfortunately these are not universal solutions because spectral filters are often specialized for specific wavelength bands and may not be suitable for co-aligned and -detected beams with widely separated wavelengths.

All modulation-based methods reject low-frequency additive noise by virtue of carrying absorption information at high modulation frequencies. All noise sources with

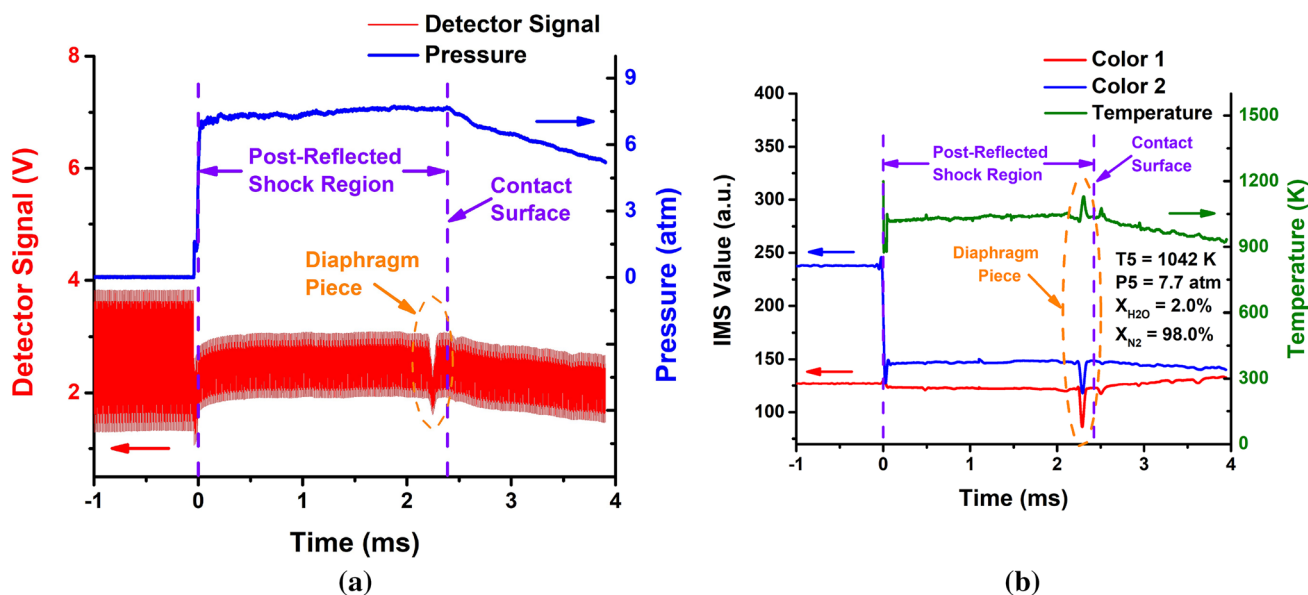


**Fig. 7** **a** Raw photodetector signal (red) and pressure trace (blue) during shock experiments at initial post-reflected shock pressure of 7.7 atm. The orange dashed circle highlights the behavior of the raw

detector signal the instant a diaphragm particle occludes the optical path. **b** Measured IMS signal values for the two lasers (blue and red) and inferred temperature (green)

temporal frequency below the lowest modulation frequency are naturally eliminated by the lock-in filtration operation. To illustrate this capability, Fig. 8 shows an IMS measurement of a pure nitrogen gas mixture (100 % N<sub>2</sub>) at reflected shock conditions of 1100 K, 11.8 atm. Due to the lack of H<sub>2</sub>O laser absorption within the shock tube, the detector signal is not expected to change with time during the experiment. However, a gradual offset (outlined in orange dotted lines in Fig. 8) in the photodetector signal caused by thermal emission in the reflected shock region was observed. If emission is not accounted for in typical direct-absorption spectroscopy techniques, the measurement will yield incorrect values for absorbance and, in turn, the desired quantities of interest. For the measurements shown in Fig. 8, the IMS signal remains essentially constant throughout the test time due to low-frequency noise rejection by the lock-in filter operation. A 38 % increase in the photodetector signal due to thermal emission translated to a 0.3 % 1 -  $\sigma$  standard deviation in the IMS signal, demonstrating the sensor's ability to reject thermal emission and other low-frequency noise sources.

### 5.3 High measurement rates

Diagnostics with sufficiently high measurement rates are needed to resolve the short thermodynamic time scales associated with practical combustion systems. The key parameter that sets the temporal resolution of modulation-based diagnostics is the modulation frequency, with higher modulation frequencies allowing for greater measurement rates. Though

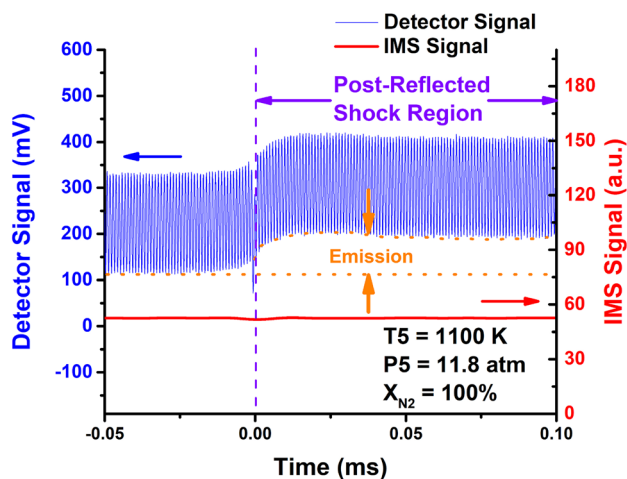


**Fig. 8** Raw photodetector signal (blue) and IMS (red) signal during a pure nitrogen shock experiment with post-reflected shock conditions of 1100 K, 11.8 atm. The orange dotted lines outline the additive offset in the photodetector signal caused by thermal emission from the hot shock tube gases. The nearly constant IMS signal demonstrate the sensor's ability to reject thermal emission and other low-frequency additive noise sources

typical WMS- $n/1f$  strategies (with  $n > 1$ ) can correct for the non-absorption losses and low-frequency additive noise sources discussed in the previous subsections just as well as the two-color IMS strategy used in this work, the inverse relationship between laser modulation depth and modulation frequency (as illustrated in Fig. 2b and generally true for semiconductor lasers) limits the maximum frequency a laser can be modulated for sensitive  $n/1f$  detection. The difficulties for using WMS- $n/1f$  are even more pronounced at high pressures due to enhanced lineshape broadening, further limiting the maximum modulation frequency and measurement rate of WMS- $n/1f$  systems. As an example, the quantum-cascade laser-based CO WMS- $2f/1f$  diagnostic demonstrated in Wei et al. [10] was set at 90 kHz modulation frequency (yielding a 45 kHz measurement as illustrated in Fig. 9a) to balance the competing needs between sensor bandwidth and adequate modulation depth for sensitive WMS- $2f/1f$  detection at high pressures. Similarly, Goldenstein et al. [28] demonstrated a WMS- $2f/1f$  sensor capable of measuring H<sub>2</sub>O and  $T$  at pressures up to 50 atm also in the HPST facility used in this work. However, due to the high modulation depth requirements needed to yield sufficient signal strength for the heavily broadened H<sub>2</sub>O spectrum at high pressures, the sensor was limited to a bandwidth of only 4.5 kHz, severely limiting the utility of such a diagnostic for reactive systems with rapid chemical timescales. Additionally, the low modulation frequencies penalize the performance of additive noise rejection via lock-in amplification.

It is also worth mentioning that pulsed-laser direct absorption technique shares some of the benefits with two-color IMS. For example, the recently developed chirped-QCL intrapulse sensing strategy described in Chrystie et al. [54] and Nasir et al. [55] can achieve spectrally resolved absorption measurements at excellent measurement rates in the order of 1 MHz. With time-division multiplexing, wavelength multiplexing can be achieved with the pulsed-laser direct absorption approach as well. Additionally, the detection principles for chirped-laser intrapulse sensing are identical to the IMS strategy presented in this work when used to measure blended spectra [56]. However, continuous-wave sources are able to provide better intensity output repeatability as compared to pulsed sources, yielding higher precision.

The two-color IMS strategy does not suffer from these limitations because IMS signals are sensitive to overall absorption rather than absorption lineshapes. But, as with any LAS sensing strategy, the accuracy of the IMS diagnostic is still dependent on the accuracy of the spectroscopic data and models at high temperatures and pressures. As a result, there are no theoretical limits to the maximum modulation frequency. With modulation frequencies of 1 MHz and 800 kHz for the two lasers used in this work, the maximum measurement bandwidth is 100 kHz as illustrated in Fig. 9b. This measurement bandwidth is sufficient to



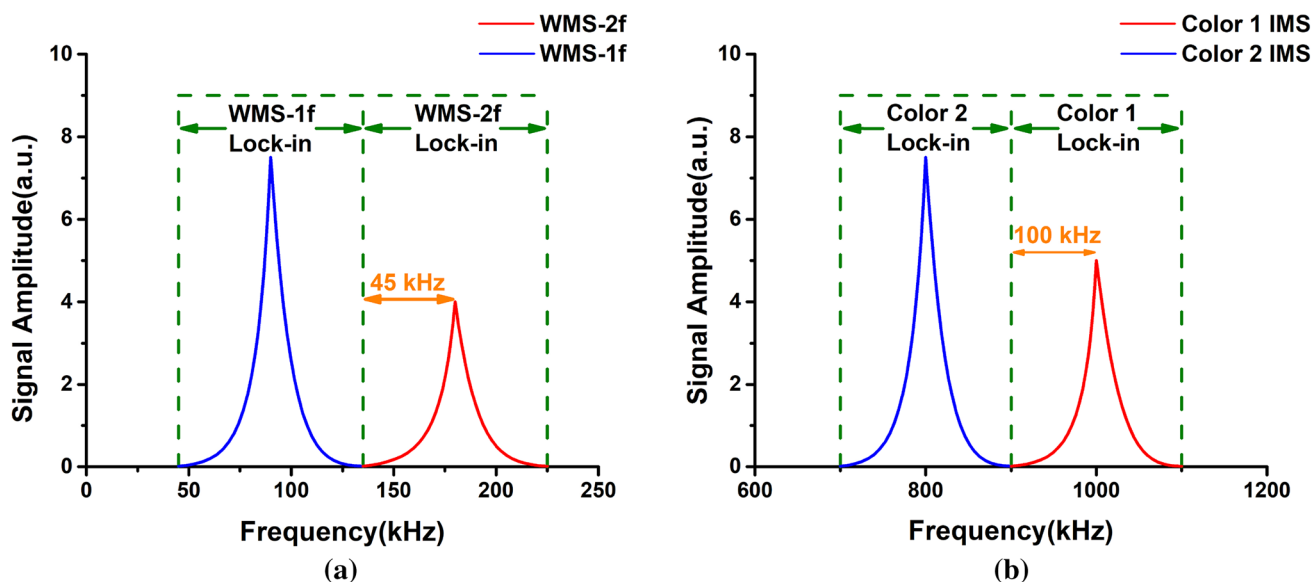


**Fig. 9** Signal intensity distribution in the frequency domain using the WMS- $2f/1f$  strategy (a) and the two-color IMS strategy (b). To achieve large sensor bandwidth, fast modulation speed is desired for

WMS- $2f/1f$ , while large modulation frequency separation is desired for two-color IMS

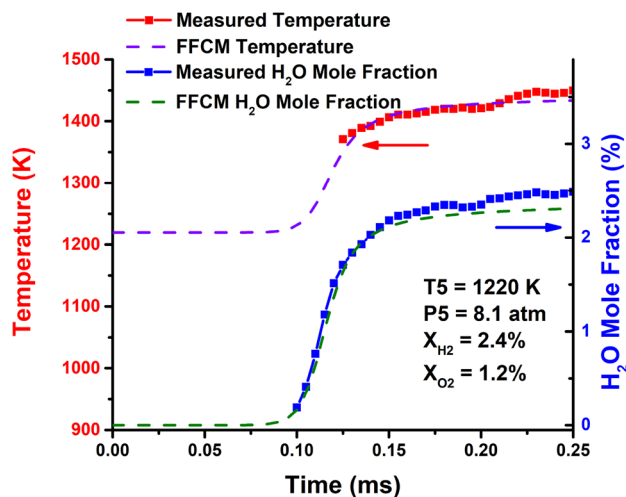


**Fig. 10** Measured temperatures and  $\text{H}_2\text{O}$  mole fractions in the post-reflected shock region of a reacting shock tube mixture initially composed of 2.4%  $\text{H}_2$ , 1.2%  $\text{O}_2$  in a  $\text{N}_2$  bath at an average post-reflected-shock temperature of 1220 K and pressure of 8.1 atm. Dashed lines are temperature and mole fraction simulations using the FFCM reaction kinetics model

resolve most combustion-relevant reaction time scales, but can be increased without bound in the future with hardware improvements discussed in Sect. 5.4.

To demonstrate the time resolution of the present two-color IMS temperature sensor, Fig. 10 shows results from a two-color IMS measurement in a reacting test gas mixture initially composed of 2.4%  $\text{H}_2$ , 1.2%  $\text{O}_2$  and  $\text{N}_2$  balance at initial

reflected shock conditions of 1220 K, 8.1 atm. With pressure known from co-located pressure transducers and assuming minimal non-absorbing losses (e.g.,  $\eta \approx 1$ ) as verified by pure  $\text{N}_2$  shocks, a variant of the temperature-measurement algorithm discussed in Goldenstein et al. [57] was used to simultaneously infer temperature and mole fraction of water from the measured IMS signals. The calculated temperature profile is shown in red and  $\text{H}_2\text{O}$  mole fraction is shown in blue with individual dots representing single-point measurements during hydrogen oxidation.

Although the hydrogen oxidation reaction is completed within a period of less than  $50 \mu\text{s}$  at initial conditions of 1220 K and 8.1 atm, the 100 kHz sensor bandwidth was able to fully resolve the  $\text{H}_2\text{O}$  mole fraction and temperature time histories.

These results were compared against simulations based on the Foundational Fuel Chemistry Model (FFCM) [58]. The close match between the measurements and FFCM simulations demonstrate the IMS sensor's capability of measuring temperature and concentration in fast chemically reacting environments. It should be noted that for the first  $20 \mu\text{s}$  (0.1 to 0.12 ms) of the experiment, the measured temperature fluctuated significantly due to the limited  $\text{H}_2\text{O}$  content and absorption during early stage combustion. Therefore, results from this period are not shown.



## 5.4 Future opportunities with the multi-color IMS technique

This work focused specifically on developing a high-bandwidth, high-precision IMS temperature diagnostic suitable for use in high-pressure shock tubes. To enable multi-species/temperature IMS diagnostics for high-pressure environments with unknown noise sources, several extensions to the sensor architecture described in this work can be pursued, some of which are described in this subsection.

*Simultaneous speciation and thermometry* As noted in Sect. 2.3, for temperature to be accurately inferred from two-color IMS experiments, either the mole fraction of the absorbing species must be precisely known or the non-absorbing transmission fraction ( $\eta$  in Eq. 8) must be close to 1. In environments where the absorbing species concentration is changing and  $\eta$  deviates from 1, a third co-aligned color can be added to the diagnostic to enable simultaneous determination of temperature, species mole fraction, and  $\eta$ . It should be noted that the third color does not need to lie within a non-absorbing region of the absorption spectrum. The third color should, however, be reasonably close to the other two colors in wavelength (to ensure that  $\eta$  does not vary significantly between the colors) and similarly free from spectral interference from other species in the test gas.

*Optical intensity modulators for extremely high sensor bandwidth and mitigation of wavelength-dependent noise sources* Acousto-optic modulators (AOM) and electro-optic modulators (EOM) are optical devices that directly modulate the intensity of a light source without perturbing the wavelength (assuming zero-chirp, radio-frequency modulation). These devices offer unique advantages that can enhance the performance of IMS sensors. First, the laser intensity can be modulated at extremely high frequencies ( $> 10$  GHz) without significant loss in intensity modulation amplitude, thus enabling extremely high measurement rates. Second, because the laser wavelength is not modulated during each intensity modulation cycle, measurement uncertainties due to wavelength-dependent noise sources such as optical étalons can be significantly mitigated. Finally, the constant laser wavelength precludes the need for accurate lineshape models—only absorption cross sections at the target wavelengths are required, which greatly simplifies the measurement post-processing procedures.

*Enhanced beam co-propagation using fiber optics and reflective optics* The success of a multi-color IMS diagnostic in rejecting non-absorption transmission losses depends on the quality of beam co-alignment and similarity in the laser spatial modes and propagation vectors of the various wavelengths prior to entering the test section. Single-mode fiber optics and fiber optic combiners provide an effective medium for spatially homogenizing the outputs from multiple lasers and thus enhancing the sensor's ability to reject

non-absorption losses. Additionally, chromatic aberrations can be eliminated from the laser transmission and detection assemblies with the use of reflective optics.

*Extension to large molecules*  $\text{H}_2\text{O}$  was the target species for this sensor due to its several advantages for combustion sensing as discussed in Sect. 3.1. However, as noted in Sect. 4.4, uncertainties in the spectroscopic parameters of water become the dominant contributors to measurement uncertainty of the IMS sensor at extreme pressures. These uncertainties can be partially alleviated through the use of large tracer molecules with numerous vibrational modes and high moments of inertia, which result in dense spectral features.

Due to this density of spectral features, the absorption spectra of large molecules are generally blended, featureless, and weakly dependent on pressure and bath gas composition at shock tube-relevant conditions [59]. It is, therefore, possible to experimentally characterize the temperature-dependent cross sections of large species at relatively low pressures that can be generalized to high pressures without significant loss in accuracy. As an example, the spectrally resolved methanol and ethanol absorption cross sections measured in Ding et al. [53] show minimal pressure dependence at pressures above 0.9 atm and at combustion-relevant temperatures near 1000 K.

These characteristics allow IMS sensor designs to leverage the known temperature-dependent absorption cross sections of large molecules (e.g., heavy hydrocarbon species commonly studied in combustion) to enable the development of temperature and species diagnostics that are less sensitive to uncertainties in spectroscopic parameters at high pressures. Additionally, these diagnostics can be successfully deployed in environments where pressure is unknown or uncertain.

## 6 Conclusions

A new two-color IMS LAS strategy with co-aligned, co-detected, and frequency-multiplexed beams was developed to measure temperature at high-pressure conditions. To the authors' knowledge, this work represents the first archival report of extending IMS-based sensing strategies for high-temperature high-pressure gas detection.

This temperature diagnostic system probed the P(16) and R(6) transitions of the fundamental asymmetric stretch rovibrational band of water near  $2.5 \mu\text{m}$ . These two transitions allowed for sensitive temperature and mole fraction measurements free from spectral interference by common combustion species. In addition to correcting for common LAS experimental difficulties (e.g., non-absorption transmission losses and low-frequency additive noise) and unlike typical WMS- $n/f/1f$  diagnostics (with  $n > 1$ ), the two-color

IMS technique remains maximally sensitive to gas absorption at high pressures and has no theoretical upper limit to the measurement bandwidth. Additionally, at sufficiently high pressures, the IMS technique becomes insensitive to uncertainties in lineshape parameters and lineshape models.

The authors believe that this sensing strategy can enable high-bandwidth measurements of temperature at pressures as high as 80 atm, where challenges such as spectral interference from adjacent transitions and other combustion species, intense beam-steering losses become dominant sources of interference that can render the sensor unusable.

This temperature diagnostic was validated at various temperature (1030–1450 K) and pressure (8–38 atm) ranges using shock tubes. For experiments near 8 atm, measured temperature time histories matched very well with calculated temperature time histories. Measurement standard deviations were calculated to be 2.9 K on average, which translates to a  $1 - \sigma$  precision of only 0.26 %. For experiments near 38 atm, measurement standard deviations were calculated to be 8.4 K on average, which translates to a  $1 - \sigma$  precision of only 0.64 % relative to the initial post-reflected shock temperature. The sensor's ability to correct for non-absorption losses, reject low-frequency additive noise from thermal emission and provide sufficiently fast measurement rates to resolve hydrogen oxidation reactions was discussed and demonstrated.

Additional modifications to the sensor architecture such as adding a third color, the use of optical intensity modulators, and fiber optics offer the capability to simultaneously measure temperature and species concentration in arbitrarily high-pressure and noisy environments in the future. The IMS technique can also be extended to other species beyond just H<sub>2</sub>O, especially large fuel molecules that are spectrally featureless and pressure insensitive even at low pressures.

**Acknowledgements** This work was supported by the Air Force Office of Scientific Research (AFOSR) with Dr. Chiping Li as technical monitor, through Grant FA9550-16-1-0195.

## References

1. A. Farooq, J.B. Jeffries, R.K. Hanson, *Appl. Opt.* **48**, 6740–6753 (2009)
2. J. Shao, R. Choudhary, D.F. Davidson, R.K. Hanson, S. Barak, S. Vasu, *Proc. Combust. Inst.* **37**, 4555–4562 (2018)
3. D.F. Davidson, J. Shao, R. Choudhary, M. Mehl, N. Obrecht, R.K. Hanson, *Proc. Combust. Inst.* **37**, 4885–4892 (2018)
4. H. Wang, R. Xu, K. Wang, C.T. Bowman, R.K. Hanson, D.F. Davidson, K. Brezinsky, F.N. Egolfopoulos, *Combust. Flame* **193**, 502–519 (2018)
5. R. Xu, K. Wang, S. Banerjee, J. Shao, T. Parise, Y. Zhu, S. Wang et al., *Combust. Flame* **193**, 520–537 (2018)
6. D.E. Burch, D.A. Gryvnak, R.R. Patty, C.E. Bartky, *J. Opt. Soc. Am.* **59**, 267–280 (1969)
7. M.Y. Perrin, J.M. Hartmann, *J. Quant. Spectrosc. Radiat. Transf.* **42**, 311–317 (1989)
8. A.G. Gaydon, I.R. Hurlle, *J. Chem. Educ.* **41**, 114 (1964)
9. J.J. Girard, R.K. Hanson, *Appl. Phys. B* **123**, 264 (2017)
10. W. Wei, W.Y. Peng, Y. Wang, R. Choudhary, S. Wang, J. Shao, R.K. Hanson, *Appl. Phys. B* **125**, 9 (2019)
11. H. Li, A. Farooq, J.B. Jeffries, R.K. Hanson, *Appl. Phys. B* **89**, 407–416 (2007)
12. R.M. Spearrin, I.A. Schultz, J.B. Jeffries, R.K. Hanson, *Meas. Sci. Technol.* **25**, 125103 (2017)
13. S. Wang, R.K. Hanson, *Opt. Lett.* **44**, 578–581 (2019)
14. R.K. Hanson, *Proc. Combust. Inst.* **33**, 1–40 (2011)
15. X. Chao, J.B. Jeffries, R.K. Hanson, *Proc. Combust. Inst.* **34**, 3583–3592 (2013)
16. W.Y. Peng, C.S. Goldenstein, R.M. Spearrin, J.B. Jeffries, R.K. Hanson, *Appl. Opt.* **55**, 9347–9359 (2016)
17. W. Wei, J. Chang, Q. Huang, Q. Wang, Y. Liu, Z. Qin, *Sens. Rev.* **37**, 2017–2024 (2017)
18. W. Wei, J. Chang, Y. Liu, X. Chen, Z. Liu, Z. Qin, Q. Wang, *Appl. Opt.* **55**, 3526–3530 (2016)
19. K. Sun, R. Sur, X. Chao, J.B. Jeffries, R.K. Hanson, R.J. Pummill, K.J. Whitty, *Proc. Combust. Inst.* **34**, 3593–3601 (2013)
20. S.T. Sanders, J.A. Baldwin, T.P. Jenkins, D.S. Baer, R.K. Hanson, *Proc. Combust. Inst.* **28**, 587–594 (2000)
21. A. Farooq, J.B. Jeffries, R.K. Hanson, *J. Quant. Spectrosc. Radiat. Transf.* **111**, 949–960 (2010)
22. H. Li, G.B. Rieker, X. Liu, J.B. Jeffries, R.K. Hanson, *Appl. Opt.* **45**, 1052–1061 (2006)
23. K. Wagatsuma, K. Hirokawa, *Anal. Chem.* **56**, 2732–2735 (1984)
24. X. Chao, J.B. Jeffries, R.K. Hanson, *Meas. Sci. Technol.* **20**, 115201–115210 (2009)
25. W.Y. Peng, R. Sur, C.L. Strand, R.M. Spearrin, J.B. Jeffries, R.K. Hanson, *Appl. Phys. B* **122**, 188 (2016)
26. W. Wei, J. Chang, Q. Wang, Z. Qin, *Sensors* **17**, 163–174 (2017)
27. W. Wei, J. Chang, Q. Huang, C. Zhu, Q. Wang, Z. Wang, G. Lv, *Appl. Phys. B* **118**, 75–83 (2015)
28. C.S. Goldenstein, R.M. Spearrin, J.B. Jeffries, R.K. Hanson, *Appl. Phys. B* **116**, 705–716 (2014)
29. M.W. Sigrist, *Infrared Phys. Technol.* **36**, 415–425 (1995)
30. A. Elia, P.M. Lugarà, C.D. Franco, V. Spagnolo, *Sensors* **9**, 9619–9628 (2009)
31. G.B. Rieker, J.B. Jeffries, R.K. Hanson, *Appl. Opt.* **48**, 5546–5560 (2009)
32. J. Shao, Y. Zhu, S. Wang, D.D. Davidson, R.K. Hanson, *Fuel* **226**, 338–344 (2018)
33. A.S. Pine, *J. Mol. Spectrosc.* **82**, 435–448 (1980)
34. P.L. Varghese, R.K. Hanson, *Appl. Opt.* **23**, 2376–2385 (1984)
35. N.H. Ngo, N. Ibrahim, X. Landsheere, H. Tran, P. Chelin, M. Schwell, J.-M. Hartmann, *J. Quant. Spectrosc. Radiat. Transf.* **113**, 870–877 (2012)
36. S.J. Cassidy, W.Y. Peng, R.K. Hanson, *J. Quant. Spectrosc. Radiat. Transf.* **221**, 172–182 (2018)
37. L. Galatry, *Phys. Rev.* **122**, 1218–1223 (1961)
38. S.G. Rautian, I.I. Sobelman, *Sov. Phys. Uspekhi.* **9**, 209–239 (1966)
39. R.J. Mathar, *J. Opt. A: Pure Appl. Opt.* **9**, 470–476 (2007)
40. L.S. Rothman, I.E. Gordon, R.J. Barber, H. Dothe, R.R. Gamache, A. Goldman, V. Perevalov, S.A. Tashkun, J. Tennyson, *J. Quant. Spectrosc. Radiat. Transfer* **111**, 2139–2150 (2010)
41. R. Sur, S. Wang, K. Sun, D.F. Davidson, J.B. Jeffries, R.K. Hanson, *J. Quant. Spectrosc. Radiat. Transfer* **156**, 80–87 (2015)
42. K. Sun, X. Chao, R. Sur, C.S. Goldenstein, J.B. Jeffries, R.K. Hanson, *Meas. Sci. Technol.* **24**, 125203 (2013)
43. Y. Wang, Y. Cao, D.F. Davidson, R.K. Hanson, *AIAA Scitech 2019 Forum*, 2248, (2019)

44. E.L. Petersen, D.F. Davidson, M. Rohrig, R.K. Hanson, Shock waves proceedings of the 20th international symposium on shock waves **2**, 941–946 (1996)
45. E.L. Petersen, D.F. Davidson, R.K. Hanson, *J. Prop. Power* **1**, 82–91 (1999)
46. D.B. Oh, M.E. Paige, D.S. Bomse, *Appl. Opt.* **37**, 2499–2501 (1998)
47. M.F. Campbell, K.G. Owen, D.F. Davidson, R.K. Hanson, *J. Thermophys. Heat Transfer* **31**, 586–608 (2017)
48. C.S. Goldenstein, I.A. Schultz, R.M. Spearrin, J.B. Jeffries, R.K. Hanson, *Appl. Phys. B* **116**, 717–727 (2014)
49. C.S. Goldenstein, J.B. Jeffries, R.K. Hanson, *J. Quant. Spectrosc. Radiat. Transfer* **130**, 100–111 (2013)
50. C.A. Almodovar, Infrared laser absorption spectroscopy of nitric oxide for sensing in high-enthalpy air (unpublished doctoral dissertation). Stanford University. Retrieved from <https://searchworks.stanford.edu/view/13330825>, (2019)
51. C.A. Almodovar, W.W. Su, C.L. Strand, R.K. Hanson, *J. Quant. Spectrosc. Radiat. Transfer* **239**, 106612 (2019)
52. C.L. Strand, Y. Ding, S.E. Johnson, R.K. Hanson, *J. Quant. Spectrosc. Radiat. Transfer* **222**, 122–129 (2019)
53. Y. Ding, C.L. Strand, R.K. Hanson, *J. Quant. Spectrosc. Radiat. Transfer* **224**, 396–402 (2019)
54. Robin S.M. Chrystie, Ehson F. Nasir, Aamir Farooq, *Proc. Combust. Inst.* **35**, 3757–3764 (2015)
55. Ehson F. Nasir, Aamir Farooq, *Opt. Express* **26**, 14601–14609 (2018)
56. R.M. Spearrin, S. Li, D.F. Davidson, J.B. Jeffries, R.K. Hanson, *Proc. Combust. Inst.* **35**, 3645–3651 (2015)
57. C.S. Goldenstein, R.M. Spearrin, J.B. Jeffries, R.K. Hanson, *Proc. Combust. Inst.* **35**, 3739–3747 (2015)
58. G.P. Smith, Y. Tao, H. Wang, Foundational fuel chemistry model version 1.0 (FFCM-1), <http://nanoenergy.stanford.edu/ffcm1>, (2016)
59. A.E. Klingbeil, J.B. Jeffries, R.K. Hanson, *Meas. Sci. Technol.* **17**, 1950–1957 (2006)

**Publisher's Note** Springer Nature remains neutral with regard to jurisdictional claims in published maps and institutional affiliations.